

Electronic Supplementary Information

Loss Compensation during Subwavelength Propagation of Enhanced Second-Harmonic Generation in Hybrid Plasmonic Waveguide

Xianqing Lin,^{a,b} Jian Ye,^a Yongli Yan,^{a,b} Haiyun Dong,^{a,b} Jianmin Gu,^a Wei Zhang,^{a,b} Cong Wei,^{a,b} Jiannian Yao,^{a,b} and Yong Sheng Zhao^{*a,b}

^aKey Laboratory of Photochemistry, Institute of Chemistry, Chinese Academy of Sciences, Beijing 100190, China. E-mail: yszhao@iccas.ac.cn

^bUniversity of Chinese Academy of Sciences, Beijing 100049, China

Contents

- 1. Experimental section**
- 2. Fig. S1.** TEM images of a single ZnSe NW.
- 3. Fig. S2.** The numerical model of HPW excited by FW laser from the top.
- 4. Fig. S3.** Schematic demonstration of the experimental setup for the optical characterization.
- 5. Fig. S4.** Estimation of second-harmonic generation conversion efficiency.
- 6. Fig. S5.** Theoretical analysis of the excitation polarization dependent SHG in ZnSe NW.
- 7. Fig. S6.** Electric field distribution in HPW under different polarized FW excitation.
- 8. Fig. S7.** Fabrication processes of different thickness of MgF₂ layer in the same substrate.
- 9. Fig. S8.** AFM image of the ZnSe NW shown in Fig. 3b.
- 10. Fig. S9.** Propagation of SHG signals achieved by angular FW excitation.
- 11. Fig. S10.** Spatial resolved spectra collected from P1 and P2 shown in Fig. 3b.
- 12. Fig. S11.** Effective indices of modes of FW and SHG signals versus the diameter of ZnSe NW in HPW.
- 13. Fig. S12.** Microscopy images of the ZnSe NW shown in Fig. 4a.
- 14. Fig. S13.** Polarization profile of the SHG signals collected from the middle and tip of the ZnSe NW shown in Fig. 4a.
- 15. Simple estimation of loss compensation efficiency of SHG signals in HPW.**

Experimental section

Preparation: The zinc selenide powder (99.99%) was purchased from Sigma Aldrich, and used without further treatment. ZnSe nanowires were synthesized with a chemical vapor deposition (CVD) method. A 300 mg ZnSe powder was placed at the center of quartz tube as the raw material. Ar (100 sccm) was used as carrier gas, while keeping the vacuum of the CVD system at ~ 200 Pa. The furnace was heated to 850 °C at a rate of 30 °C/minute and kept at that temperature for 1 hour. After the furnace was naturally cooled to the room temperature, the substrates coated with ZnSe nanowires were obtained. Then, the ZnSe nanowires were deposited from solution by casting onto the silver substrates with differing MgF₂ layers thickness of 5, 10, 15, 20, 25, 30, 40, 50 nm. As a result, the ZnSe nanowire hybrid plasmonic waveguide structures were obtained.

Structural and morphological characterization: The nanowires were transferred onto different substrates for the measurements of scanning electron microscopy (SEM, Hitachi, S-4800), transmission electron microscopy (TEM, JEOL, 2100F) and atomic force microscopy (AFM Bruker Multimode 8).

Optical measurements: The schematic demonstration of the experimental setup for optical characterization is shown in Fig. S3. Bright-field and SH microscopy images were taken with an inverted microscope (Nikon, Ti-U). To measure the SH spectra, the ZnSe NW was excited locally with a Ti:sapphire laser (Chameleon Vision II) focused down to the diffraction limit through an objective (Nikon CFLU Plan, 50x, N.A.=0.8; CFLU Plan, 100x, N.A.=0.9). The polarization of FW signals was altered with a half wave plate. The emission from the ZnSe NW was dispersed with a grating (150 G/mm) and recorded with a thermal-electrically cooled CCD (Princeton Instruments, ProEm: 1600B).

Numerical simulation: The numerical simulations were carried out with the commercial software Comsol, and the frequency domain Wave Optics module was employed. A hexagonal prism was used to model ZnSe NW with a refractive index (n) of 2.5 (Fig. S2). The thickness of the Ag film is 1 μm with a permittivity of $-35.585+0.47724i$ at wavelength of 850 nm and $-5.7687+0.20754i$ at wavelength of 425 nm, respectively. The height (h) of the calculated MgF₂ layers ($n=1.38$) was varied from 5 nm to 50 nm with 5 nm intervals.

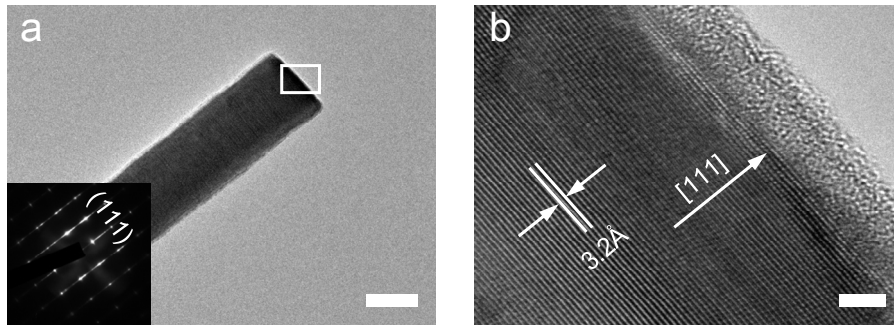


Fig. S1. TEM images of a single ZnSe nanowire. (a) TEM image of a typical ZnSe NW. Inset: selected area electron diffraction of the nanowire. Scale bar is 100 nm. (b) High-resolution TEM image of the selected area shown in (a). Scale bar is 3 nm.

As shown in Fig. S1, the selected area electron diffraction (SAED) taken from a nanowire reveals that the ZnSe NW is a single crystal grown along [111] direction with zinc blende crystal structure. Due to the cubic tetrahedral symmetry restrictions, the first hyperpolarizability tensor components $\beta_{xyz}=\beta_{yzx}=\beta_{zxy}$ (That is, the second-order nonlinear optical susceptibility parameters are equal ($d_{14}=d_{25}=d_{36}$)) survive. Therefore, the as-prepared ZnSe NW is favorable for the efficient SH radiation.¹

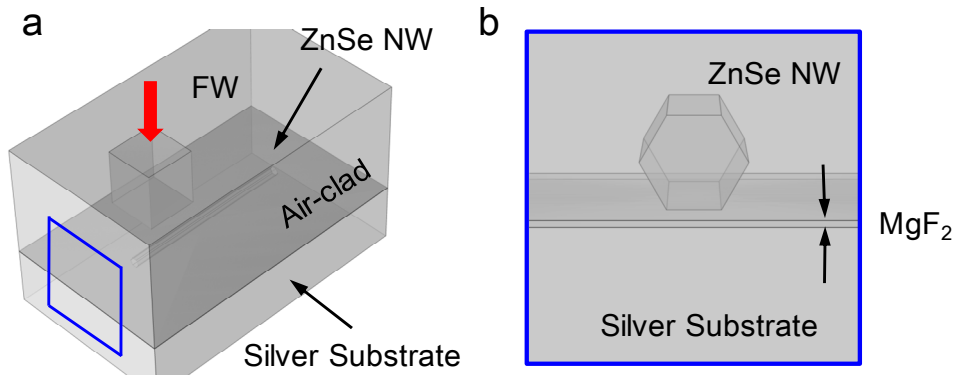


Fig. S2. The numerical model of HPW excited by FW laser from the top. (a, b) 3D full view (a) and side-view (b) of the numerical model of HPW. The numerical simulations of the electric field distribution were carried out using the commercial software COMSOL, which can solve three dimensional Maxwell equations by the finite element method. A hexagonal prism was used to model ZnSe NW with a refractive index (n) of 2.5. The thickness of the Ag film is 1 μm with a permittivity of $-35.585+0.47724i$ at wavelength of 850 nm and $-5.7687+0.20754i$ at wavelength of 425 nm, respectively. The height (h) of the calculated MgF₂ layers ($n=1.38$) was varied from 5 nm to 50 nm with 5 nm intervals. The HPW was illuminated by a linearly polarized beam from the top.

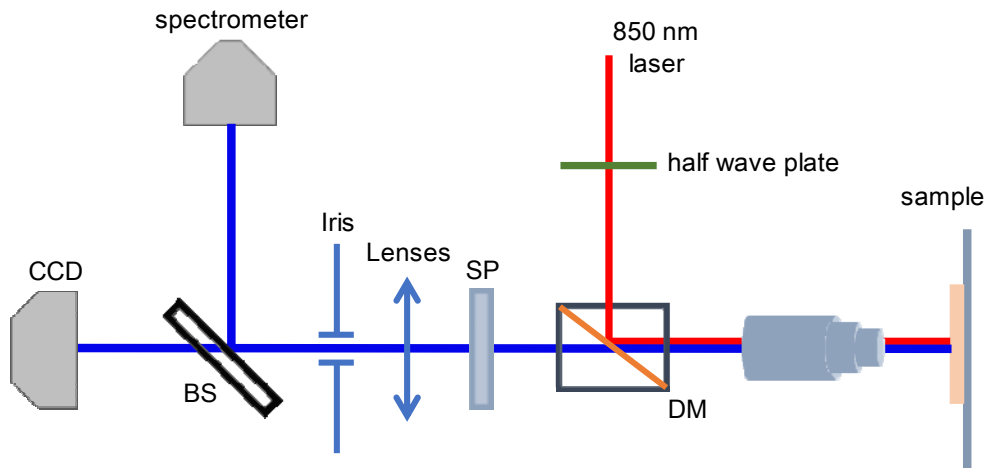


Fig. S3. Schematic demonstration of the experimental setup for the optical characterization. Bright-field and SH microscopy images were taken with an inverted microscope (Nikon, Ti-U). To measure the SH spectra, the ZnSe NW was excited locally with a Ti:sapphire laser (Chameleon Vision II) focused down to the diffraction limit through an objective (Nikon CFLU Plan, 50x, N.A.=0.8; CFLU Plan, 100x, N.A.=0.9). The polarization of FW signals was altered with a half wave plate. The emission from the ZnSe NW was dispersed with a grating (150 G/mm) and recorded with a thermal-electrically cooled CCD (Princeton Instruments, ProEm: 1600B).

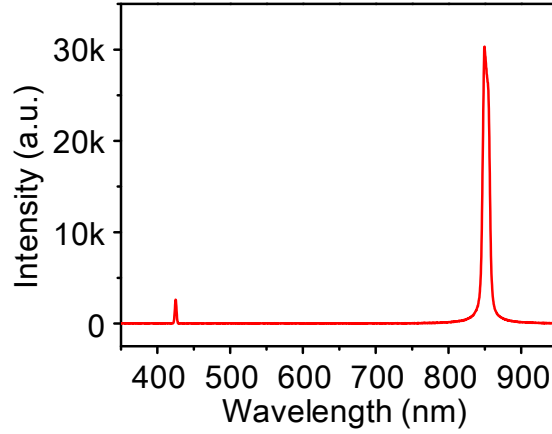


Fig. S4. Estimation of second-harmonic generation conversion efficiency. The spectrum of the reflected SHG signals (425 nm) and the corresponding pumping laser (850 nm). The intensity of the pumping laser was attenuated by a 750 nm short pass filter before collected by the spectrometer.

Fig. S4 shows the spectrum taken from a single ZnSe nanowire (NW) in HPW structure with 10 nm thick MgF₂ layer. A dichroic mirror (805 nm short pass) and short pass filter (750 nm) were placed in front of the spectrometer to attenuate the pumping laser before collected by the spectrometer. The small peak centered at 425 nm corresponds to the SHG signals, while the higher peak centered at 850 nm is attributed to the FW signals. The conversion efficiency (η) of enhanced SHG in HPW was estimated according to the following equation:²

$$\eta = \frac{Q_{FW}}{Q_{SHG}} \cdot \frac{T_{FW(DM)}}{T_{SHG(DM)}} \cdot \frac{T_{FW(SP)}}{T_{SHG(SP)}} \cdot \frac{S_{FW}}{S_{SHG}} \cdot \frac{I_{SHG}}{I_{FW}}$$

where Q_{FW} and Q_{SHG} correspond to the collective efficiency of spectrometer for the wavelength of FW and SHG signals; $T_{FW(DM)}$ ($T_{SHG(DM)}$) and $T_{FW(SP)}$ ($T_{SHG(SP)}$) are transmittance of 805 nm short pass dichroic mirror and 750 nm short pass filter for the wavelength of FW (SHG) signals, respectively. The above ratios are listed in Table S1, which can be obtained in product manuals.³⁻⁵ S_{FW} is the area of the focal spot and S_{SHG} is attributed to the area of NW within the laser spot. I_{SHG} and I_{FW} are obtained from the measured spectrum demonstrated in Fig. S4. According to the equation, the SHG conversion efficiency is estimated to be $5 \times 10^{-6}\%$ under the pump power of 5 mW.

Table S1. The ratio values for the simple estimation of SHG conversion efficiency

Q_{FW}/Q_{SHG}	$T_{FW(DM)}/T_{SHG(DM)}$	$T_{FW(SP)}/T_{SHG(SP)}$	S_{FW}/S_{SHG}	I_{SHG}/I_{FW}
0.57/0.69	0.585/88.9	$2.13 \times 10^{-4}/56.2$	$2.5\pi/0.32$	2602/30328

Table S2. The conversion efficiencies of SHG in different micro-/nanostructures

Material	Size	Conversion efficiency	Reference
GaAs	5 μm	$5 \cdot 10^{-5}$	<i>Nat. Commun.</i> , 2014, 5 , 3109
CdTe	800 nm	10^{-10}	<i>Nano Lett.</i> , 2016, 16 , 4807-4810
GaP	150 nm	$2 \cdot 10^{-9}$	<i>Nano Lett.</i> , 2012, 12 , 820-826
CdS/Au	1 μm	$2 \cdot 10^{-8}$	<i>ACS Nano</i> , 2015, 9 , 5018-5026
CdS/Ag	230 nm	$3 \cdot 10^{-6}$	<i>Nat. Commun.</i> , 2014, 5 , 5432
Silica/Au	120 nm	$1.8 \cdot 10^{-9}$	<i>Nano Lett.</i> , 2011, 11 , 5519-5523
Au	1 μm	$1.25 \cdot 10^{-9}$	<i>Nano Lett.</i> , 2012, 12 , 4997-5002

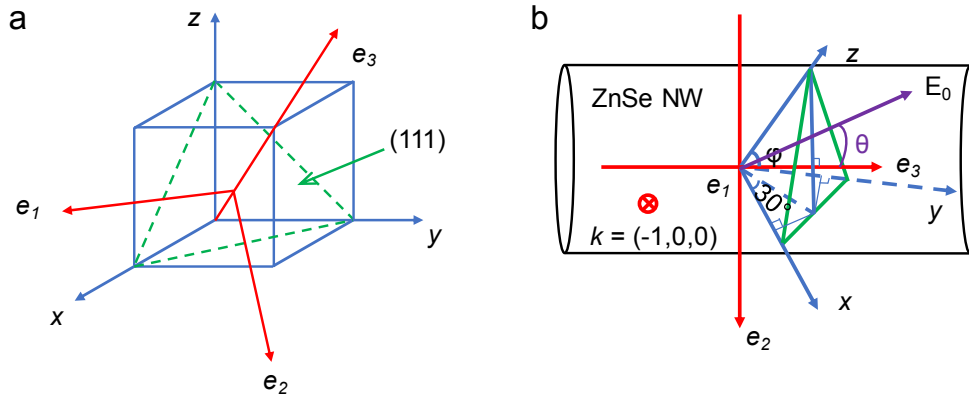


Fig. S5. Theoretical analysis of the excitation polarization dependent SHG in ZnSe nanowire. (a) Illustration of the growth structure of the ZnSe nanowire. (x, y, z) is the crystal coordinate while (e_1, e_2, e_3) is the laboratory coordinate. The green triangle is the (111) plane of ZnSe nanowire and the nanowires is grown along e_3 direction, which is perpendicular to (111) plane. (b) The relative angles between the crystal coordinate and laboratory coordinate. We presume that the FW radiated along the e_1 direction to simplify the calculation and the wave vector of the pumping laser is along $(-1,0,0)$ direction. As a result, E_0 has an angle of θ with respect to the e_3 axis.

ZnSe nanowire has a zinc blende crystal structure and belongs to the point group $\bar{4}3m$. The ZnSe nanowires grow along $[111]$ direction, as shown in Fig. S5a. The two coordinate systems are established on the crystal axes (x, y, z) (blue lines) and the laboratory coordinate system (e_1, e_2, e_3) (red lines), respectively. The laboratory axis e_3 has an angle of ϕ with the crystal axes. To simplify the calculation, we just take two specified conditions (TM-polarized and TE-polarized FW excitation) into consideration.

Under TM-polarized FW excitation ($E//e_3, \theta=0^\circ$), the three components of the electric field E_0 in xyz system can be written as (see Fig. S5b):

$$E_x = E_y = E_z = E_0 \cos \varphi. \quad (S1)$$

When the FW is polarized perpendicular to the long-axis of ZnSe nanowire (That is TE-polarized FW excitation, $E//e_2, \theta=90^\circ$), the components of E_0 at (x, y, z) coordinate can be described as:

$$E_x = E_y = \gamma_{\omega,in} E_0 \cos 30^\circ \cos \varphi \quad (S2)$$

$$E_z = \gamma_{\omega,in} E_0 \sin \varphi \quad (S3)$$

where $\gamma_{\omega,in}$ stands for the in-coupling coefficient of the electric field which is polarized perpendicular to the nanowire.

According to the equation $P_i(2\omega) = \varepsilon_0 \sum_{jk} \chi_{ijk}^{(2)} E_j(\omega) E_k(\omega)$ and the ($\bar{4}3m$) crystal of ZnSe nanowire, the polarization components can be expressed as:

$$\vec{P} = \varepsilon_0 \begin{bmatrix} 0 & 0 & 0 & d_{14} & 0 & 0 \\ 0 & 0 & 0 & 0 & d_{14} & 0 \\ 0 & 0 & 0 & 0 & 0 & d_{14} \end{bmatrix} \cdot \begin{bmatrix} E_x(\omega)^2 \\ E_y(\omega)^2 \\ E_z(\omega)^2 \\ 2E_y(\omega)E_z(\omega) \\ 2E_x(\omega)E_z(\omega) \\ 2E_x(\omega)E_y(\omega) \end{bmatrix} \quad (S4)$$

Substituting Eq. (S1) into Eq. (S4),

$$\vec{P}(\theta = 0^\circ) = \begin{bmatrix} 2\varepsilon_0 d_{14} E_0^2 \cos^2 \varphi \\ 2\varepsilon_0 d_{14} E_0^2 \cos^2 \varphi \\ 2\varepsilon_0 d_{14} E_0^2 \cos^2 \varphi \end{bmatrix}. \quad (S5)$$

When Eq. (S2) and Eq. (S3) were substituted into Eq. (S4), the polarization is given by the expression:

$$\vec{P}(\theta = 90^\circ) = \begin{bmatrix} \sqrt{3}\varepsilon_0 d_{14} \gamma_{\omega,in}^2 E_0^2 \sin \varphi \cos \varphi \\ \sqrt{3}\varepsilon_0 d_{14} \gamma_{\omega,in}^2 E_0^2 \sin \varphi \cos \varphi \\ \frac{3}{2}\varepsilon_0 d_{14} \gamma_{\omega,in}^2 E_0^2 \cos^2 \varphi \end{bmatrix}. \quad (S6)$$

Therefore, the intensities of SHG under different polarizations of FW excitation are

$$I(\theta = 0^\circ) = |P|^2 = 12\varepsilon_0^2 d_{14}^2 E_0^4 \cos^4 \varphi, \quad (S7)$$

$$I(\theta = 90^\circ) = |P|^2 = 6\varepsilon_0^2 \gamma_{\omega,in}^4 d_{14}^2 E_0^4 \sin^2 \varphi \cos^2 \varphi + \frac{9}{4}\varepsilon_0^2 \gamma_{\omega,in}^4 d_{14}^2 E_0^4 \cos^4 \varphi. \quad (S8)$$

Consequently, the ratio of SHG signals intensities ($I(\theta=0^\circ)/I(\theta=90^\circ)$) is

$$\begin{aligned} \frac{I(\theta=0^\circ)}{I(\theta=90^\circ)} &= \frac{12\varepsilon_0^2 d_{14}^2 E_0^4 \cos^4 \varphi}{6\varepsilon_0^2 \gamma_{\omega,in}^4 d_{14}^2 E_0^4 \sin^2 \varphi \cos^2 \varphi + \frac{9}{4}\varepsilon_0^2 \gamma_{\omega,in}^4 d_{14}^2 E_0^4 \cos^4 \varphi} \\ &= \frac{12d_{14}^2 \cos^2 \varphi}{6\gamma_{\omega,in}^4 d_{14}^2 \sin^2 \varphi + \frac{9}{4}\gamma_{\omega,in}^4 d_{14}^2 \cos^2 \varphi}. \end{aligned} \quad (S9)$$

As we can see from the Eq. (S9), both the the anisotropic second-order coefficient of ZnSe NW (which is reflected by $d_{14}^2 \cos^2 \varphi$ and $d_{14}^2 \sin^2 \varphi$ in the equation.) and the size-dependent in-coupling coefficient ($\gamma_{\omega,in}$) contribute to the polarization anisotropy of SHG signals in ZnSe NW.

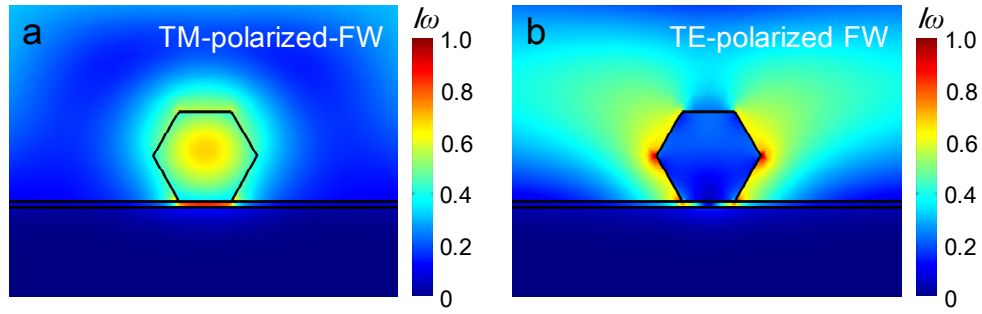


Fig. S6. Electric field distribution in HPW under TM-polarized (a) and TE-polarized (b) FW excitation.

As we can see, due to the size-dependent in-coupling coefficient effect, much stronger electric field is confined in ZnSe NW under TM-polarized FW excitation than that excited by TE-polarized FW. Moreover, compared with the weak field confinement in HPW excited by TE-polarized FW, much more sufficient electric field confinement in the gap region between the nanowire and metal surface was achieved under TM-polarized FW excitation. This can be ascribed to the highly polarized behavior of the hybrid plasmonic mode in HPW. As a result, polarization anisotropy of SHG signals was enhanced in HPW.

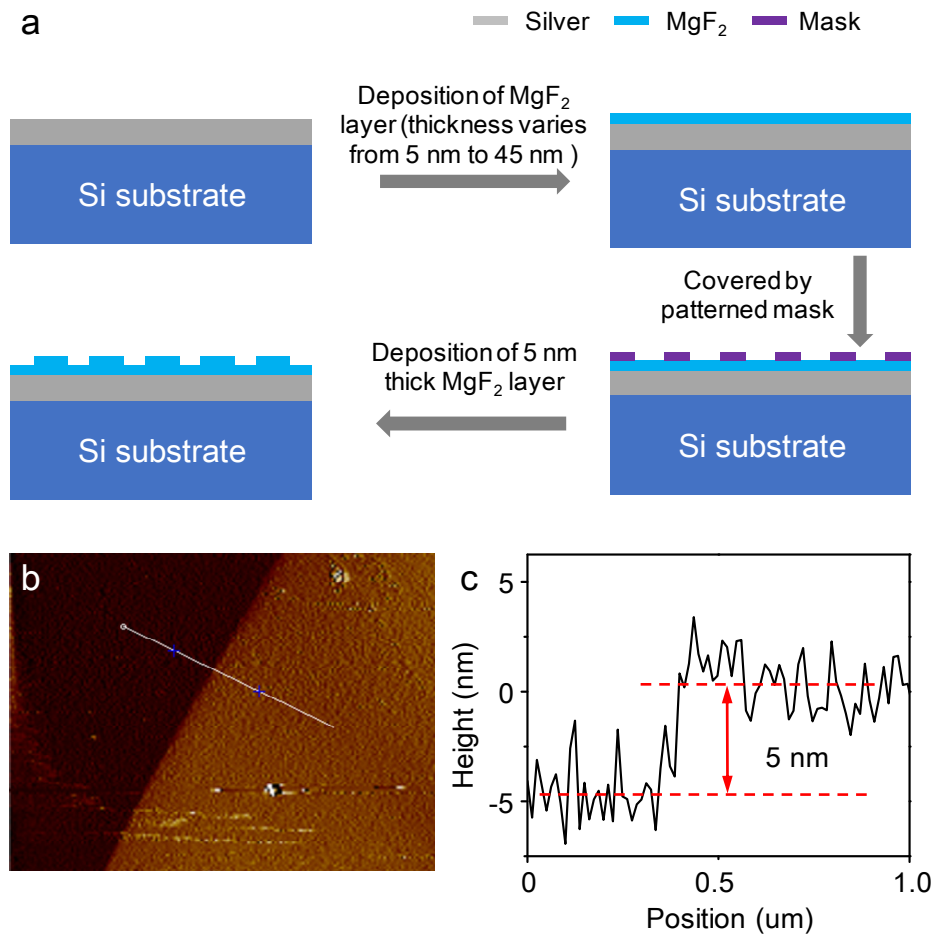


Fig. S7. Fabrication processes of different thickness of MgF₂ layer in the same substrate. (a) Schematic demonstration of the fabrication processes. (b, c) AFM image and cross-section profile of different thickness of MgF₂ layer.

As illustrated in Fig. S7, multistep deposition process was conducted to obtain two different thickness of MgF₂ layer in the same substrate. Firstly, MgF₂ layer (the thickness can be varied from 5 nm to 45 nm with 5 nm intervals) was deposited after the deposition of silver layer on the flat silicon substrates. Then the substrates were covered with patterned mask. Finally, another 5 nm thick MgF₂ layer was deposited onto the covered substrates. As shown in Fig. S7b,c, the as-prepared substrate has clear boundary between the two deposited MgF₂ layers.

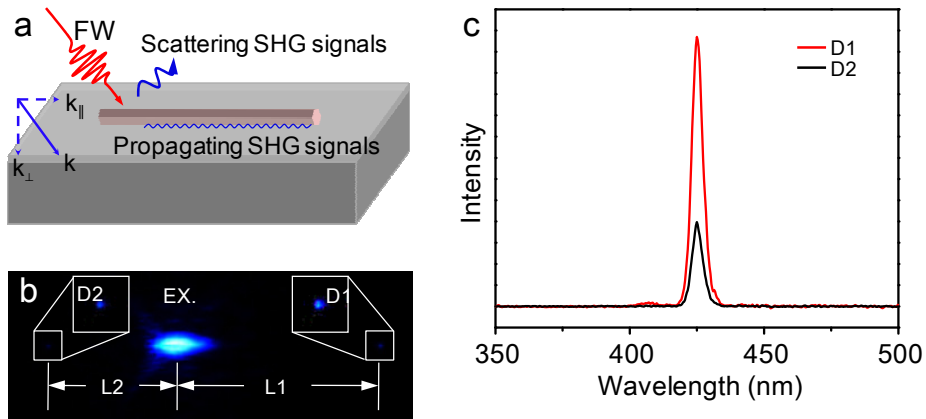


Fig. S8. Propagation of SHG signals achieved by angular FW excitation. (a) Schematic illustration of angular FW excitation. D1 and D2: the two distal ends of nanowire; k : momentum of incident FW laser, k_{\perp} and $k_{//}$ correspond to k -vector component perpendicular and parallel to metal surface. (b) SH image of a typical HPW generated from angular FW excitation. L1 and L2: the propagation distance from excitation spot to D1 and D2, respectively. (c) Spatial resolved spectra collected from D1 and D2 shown in (b).

It can be seen that the generated SHG signals were guided towards two opposite ends (D1, D2) of the wire. Spatial resolved spectra collected from D1 and D2 show that the light outcoupled from D1 is stronger than that from D2 in spite of longer propagation distance ($L1 > L2$, illustrated in Fig. S4b). These results reveal that angular FW excitation is profitable to obtain subwavelength waveguiding of SHG signals.

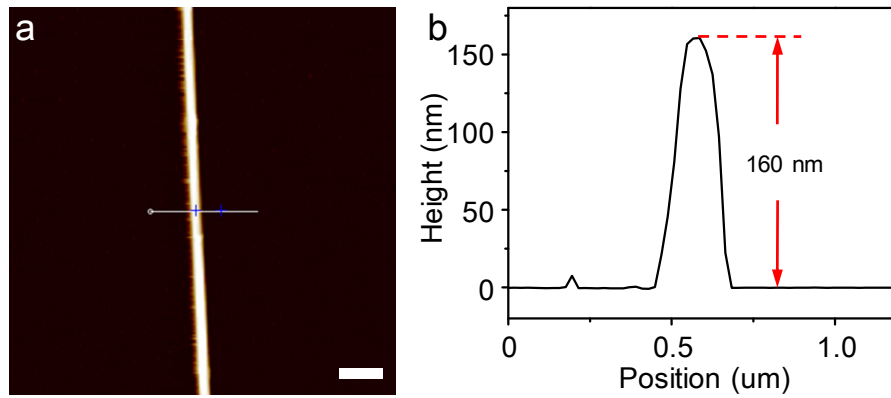


Fig. S9. AFM image of the ZnSe NW shown in Fig. 3b. (a, b) AFM image and cross-section profile of the ZnSe NW shown in Fig. 3b. The diameter of nanowire is about 160 nm. Scale bar is 400 nm.

We can see that the diameter of ZnSe NW is about 160 nm. Therefore, the phase matching between the fundamental mode at the FW and second-order mode at the SH (Fig. 3a) becomes possible for the HPW with 160-nm-diameter ZnSe NW. As a result, coherent loss compensation can be achieved through the efficient energy upconversion of FW signals, which is beneficial for the subwavelength waveguiding of SHG signals in HPW.

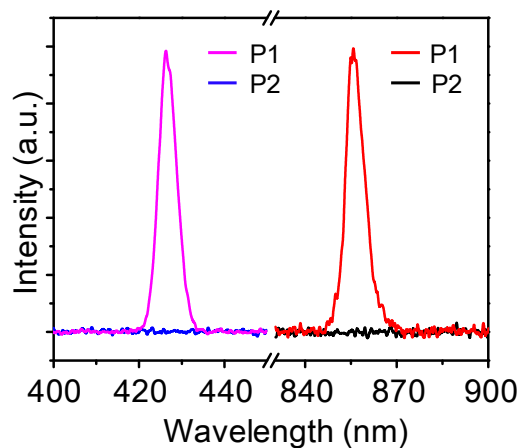


Fig. S10. Spatial resolved spectra collected from P1 and P2 shown in Fig. 3b.

The spatial resolved spectra show that both FW and SHG signals were detected at P1. In sharp contrast, no measurable signal was acquired from P2, which excludes the possibility of scattering signals from the excitation point. This indicates that the signals obtained from P1 were resulted from the propagation of FW and SHG signals in HPW.

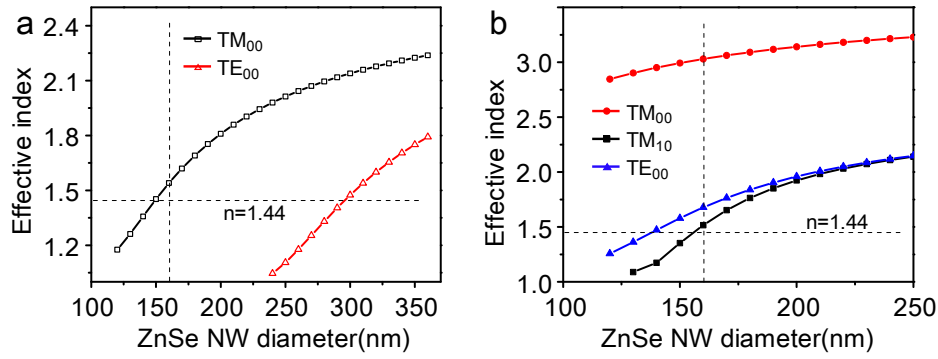


Fig. S11. Effective indices of the optical modes of FW and SHG signals versus the diameter of ZnSe NW in HPW. (a, b) Effective indices of the optical modes of FW signals (a) and SHG signals (b) versus the diameter of ZnSe NW. The horizontal dash lines shown in (a, b): the cut-off effective index is 1.44; The vertical dash lines shown in (a, b): the diameter of ZnSe is 160 nm.

Owing to the cut-off effect in HPW, only one TM-polarized hybrid plasmonic mode of FW signals can be supported in HPW if the diameter of ZnSe NW is 160 nm (Fig. S7a, dash line). On the contrary, there are three optical modes of SHG signals (hybrid plasmonic modes (marked as TM_{00} , TM_{10}) and dielectric waveguide mode (TE_{00})) with the refractive index larger than 1.44 (Fig. S7b) existed if the diameter of ZnSe NW is 160 nm. In HPW structure, the electric field normal to the metal surface shows the strongest coupling to SPP,⁶ so that the emission at the waveguide point would exhibit highly polarized along the long-axis of nanowire after the waveguiding. This provides an efficient way to distinguish the hybrid plasmonic waveguiding from the dielectric waveguiding with the polarization of the signals outcoupled from the waveguide point.

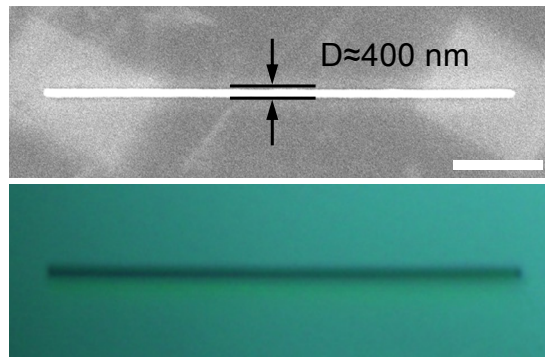


Fig. S12. Microscopy images of the ZnSe NW shown in Fig. 4a. SEM (top) and bright-field (bottom) images of the corresponding sample shown in Fig. 4a. The diameter of ZnSe NW is about 400 nm. Scale bar is 4 μm .

It can be seen that the diameter of ZnSe NW is about 400 nm. Therefore, two TM-polarized hybrid plasmonic modes (Fig. 4c,d) would be supported in the 400-nm-diameter ZnSe HPW structure. During the subwavelength waveguiding of different hybrid plasmonic modes, constructive interference will be obtained due to the different propagation constants between them. As a result, periodic patterns of SHG signals emerge along the ZnSe NW, which will help to better understand the loss-compensated waveguiding of SHG signals in HPW.

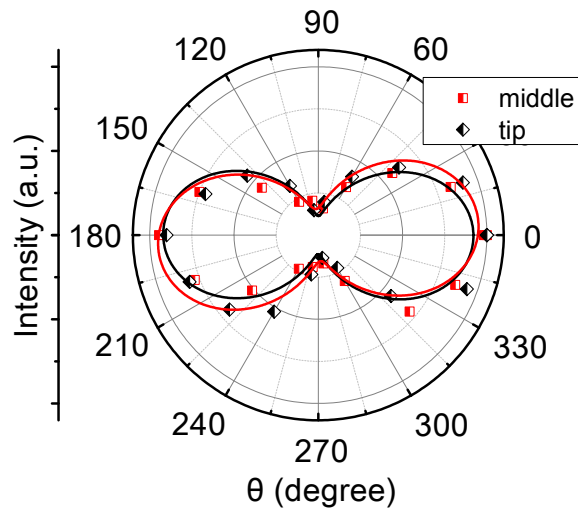


Fig. S13. Polarization profile of the SHG signals collected from tip and middle of the ZnSe NW shown in Fig. 4a.

Both the signals acquired from the tip and middle of the 400-nm-diameter ZnSe NW are parallel polarized to the long-axis of the nanowire (that is, TM-polarized), which is consistent with that obtained from the 160-nm-diameter ZnSe NW HPW structure. This indicates that the periodic SH radiation should be resulted from the interference of different hybrid plasmonic modes of FW signals during the waveguiding, which is helpful to gain deeper insights into the subwavelength waveguiding of SHG signals in HPW.

Simple estimation of loss compensation efficiency of SHG signals in HPW

In HPW structure, for FW signals, the propagation losses can be roughly divided into three types: a) the intrinsic losses of hybrid plasmonic mode arising from absorption in the metal; b) the scattering losses caused by the roughness of the surfaces (including the surfaces of the substrate and ZnSe NW); c) the upconversion of FW during the waveguiding. Thus, the optical-loss coefficient (R_ω) obtained from the experiments can be expressed as:

$$R_\omega = R_{SPP,\omega} + R_{scattering} + R_{upconversion} \quad (S10).$$

For SHG signals, the propagation losses can also be divided into three types: a) the intrinsic losses of hybrid plasmonic mode; b) the scattering losses; c) the compensation generated from the upconversion of FW during the waveguiding. Therefore, the optical-loss coefficient ($R_{2\omega}$) can be written as:

$$R_{2\omega} = R_{SPP,2\omega} + R_{scattering} + G_{compensation} \quad (S11).$$

As the relationship between the new generated SHG signals and upconverted FW signals can be given by equation: $I_{SHG} \propto I_{FW}^2$, so that $|R_{upconversion}| = 2|G_{compensation}|$. To roughly estimate the loss compensation efficiency of SHG signals in HPW, we assume that the scattering losses of FW and SHG signals are equal. Therefore, according to the equation, the loss compensation efficiency is estimated to be $0.05 \text{ dB } \mu\text{m}^{-1}$.

Table S3. The values for the simple estimation of loss compensation efficiency

R_ω	$R_{SPP,\omega}$	$R_{2\omega}$	$R_{SPP,2\omega}$
$0.2 \text{ dB } \mu\text{m}^{-1}$	$0.02 \text{ dB } \mu\text{m}^{-1}$	$0.51 \text{ dB } \mu\text{m}^{-1}$	$0.54 \text{ dB } \mu\text{m}^{-1}$

References

- 1 R. Cisek, D. Tokarz, N. Hirmiz, A. Saxena, A. Shik, H. E. Ruda and V. Barzda, *Nanotechnology* 2014, **25**, 505703.
- 2 H. Hu, K. Wang, H. Long, W. Liu, B. Wang and P. Lu, *Nano Lett.* 2015, **15**, 3351-3357.
- 3 <http://www.thorlabs.hk/thorproduct.cfm?partnumber=DMSP805>.
- 4 <http://www.thorlabs.hk/thorproduct.cfm?partnumber=FES0750>.
- 5 <http://www.princetoninstruments.com/products/ProEM-EMCCD>.
- 6 Q. Zhang, G. Li, X. Liu, F. Qian, Y. Li, T. C. Sum, C. M. Lieber and Q. Xiong, *Nat. Commun.* 2014, **5**, 4953.